Preprint Title	Design aspects of $Bi_2Sr_2CaCu_2O_{8+\delta}$ THz sources: optimization of thermal and radiative properties
Authors	Mikhail M. Krasnov, Natalia D. Novikova, Roger Cattaneo, Alexey A. Kalenyuk and Vladimir M. Krasnov
Publication Date	01 Oct 2021
Article Type	Full Research Paper
ORCID® iDs	Vladimir M. Krasnov - https://orcid.org/0000-0002-3131-8658

Design aspects of $Bi_2Sr_2CaCu_2O_{8+\delta}$ THz sources: optimization of thermal and radiative properties

Mikhail M. Krasnov[1,2], Natalia D. Novikova[1,2], Roger Cattaneo[3], Alexey A. Kalenyuk[3,4,5] and Vladimir M. Krasnov*[2,3]

Address: [1]Keldysh Institute of Applied Mathematics of RAS, Moscow, Russia; [2]Moscow Institute of Physics and Technology, 141700 Dolgoprudny, Russia; [3]Department of Physics, Stockholm University, AlbaNova University Center, SE-10691 Stockholm, Sweden; [4]Institute of Metal Physics of National Academy of Sciences of Ukraine, 03142 Kyiv, Ukraine and [5]Kyiv Academic University, 03142 Kyiv, Ukraine

Email: Vladimir M. Krasnov - vladimir.krasnov@fysik.su.se

* Corresponding author

Abstract

Impedance matching and heat management are important factors influencing performance of THz sources. In this work we analyze thermal and radiative properties of such devices based on mesa structures of a layered high-temperature superconductor $Bi_2Sr_2CaCu_2O_{8+\delta}$. Two types of devices are considered, containing either a conventional large single crystal, or a whisker. We perform numerical simulations for various geometrical configurations and parameters and make a comparison with experimental data for the two types of devices. It is demonstrated that the structure and the geometry of both the superconductor and the electrodes are playing important roles. In crystal-based devices an overlap between the crystal and the electrode leads to appearance of a large parasitic

capacitance, which shunts THz emission and prevents impedance matching with open space. The overlap is avoided in whisker-based devices. Furthermore, the whisker and the electrodes form a turnstile (crossed-dipole) antenna facilitating good impedance matching. This leads to more than an order of magnitude enhancement of the radiation power efficiency in whisker-based, compared to crystal-based devices. These results are in good agreement with presented experimental data.

Keywords

Terahertz sources; Josephson junctions; High-temperature superconductivity; Numerical modelling;

Introduction

Low radiation power efficiency is a key problem of terahertz (THz) sources of electromagnetic waves (EMW), colloquially known as “the THz gap" [1]. Tunable, monochromatic, continuous-wave (CW), compact and power-efficient THz sources are required for a broad variety of applications [1]. However, their radiation power efficiency (RPE) is rapidly decreasing with decreasing frequency. Despite a remarkable progress achieved by semiconducting quantum cascade lasers (QCL’s) [2,3], their RPE drops well below a percent level at low THz frequencies [4-6]. Furthermore, operation of QCL is limited by thermal smearing of quantum levels, which becomes significant at frequencies $f \lesssim k_B T/h$, where k_B and h are Boltzmann and Planck constants and T is the operation temperature. For room temperature, $T = 300$ K, this frequency is $f \simeq 6.25$ THz. QCL’s have to be cooled down in order to operate at significantly lower primary frequencies [4-6]. Although room temperature operation of QCL’s at low frequencies can be achieved via mixing and down conversion of the higher primary frequency, this comes at the expense of a dramatic reduction of RPE [2,3,5,7,8].

Layered high-temperature superconductor $Bi_2Sr_2CaCu_2O_{8+\delta}$ (Bi-2212) may provide an alternative technology for creation of cryogenic THz sources [9-21]. Bi-2212 represents a natural stack of atomic scale intrinsic Josephson junctions (IJJ’s) [22-25]. Josephson junctions have an inherently tunable oscillation frequency, $f_J = (2e/h)V$, where e is electron charge and V is the bias voltage per junction. The frequency is limited only by the superconducting energy gap, which can be in excess of 30 THz for Bi-2212 [26,27]. A broad range tunability of emission in the whole THz range $1 - 11$ THz has been demonstrated from small Bi-2212 mesa structures [14].

Operation of Josephson emitters is limited by two primary obstacles: self-heating and impedance matching. Josephson devices stop operating when their temperature exceeds the superconducting critical temperature T_c. Self-heating in Bi-2212 mesa structures has been intensively studied [27-36]. Although T_c of Bi-2212 may be quite high, up to $\simeq$ 95 K [27], self-heating is substantial due to a low heat conductance of superconductors. Self heating limits the maximum bias voltage that can be reached without critical overheating of the mesa and, therefore, the maximum achievable frequency and the emission power. Furthermore, as pointed out in Ref. [37], self-heating creates a general limitation for the maximal achievable emission power for any cryogenic device (not only superconducting). Taking into account the limited cooling power of compact cryo-refrigerators (sub-Watt at low T), a device with RPE $\sim$ 1% would not be able to emit significantly more than 1 mW. Therefore, larger emission power from cryogenic sources may only be achieved via enhancement of RPE. The maximum achievable RPE is 50% in the case of perfect matching of the device microwave impedance with that for open space [38]. However, the reported RPE of Bi-2212 THz sources is much smaller [14] due to a significant impedance mismatch. Therefore, improvement of THz sources requires proper design of cooling elements to handle self-heating, and impedance matching microwave antennas, to improve RPE.

In this work we analyze design aspects of THz sources based on Bi-2212 mesa structures. Thermal and radiative properties are studied for two types of devices containing either a conventional large single crystal, or a whisker. We present numerical simulations for various geometrical configurations and parameters and make a comparison with experimental data. It is demonstrated that the structure and the geometry of both the superconductor and the electrodes are playing important roles. Electrodes provide an effective heat sink channel and help in reduction of self-heating. They also influence radiative properties. However, this influence is opposite for crystal-based (worsen) and whisker-based (improve) devices. The superconductor geometry is also crucial. Devices based on large crystals suffer from a large parasitic capacitance at the overlap between the crystal and the electrodes. It prevents good impedance matching and reduces RPE. The overlap is avoided in whisker-based devices. Moreover, the whisker itself, together with electrodes, forms a turnstile (crossed-dipole) antenna, facilitating good impedance matching. We show that this leads to more that an order of magnitude enhancement of RPE, compared to crystal-based devices. Those results are in good agreement with experimental data, which demonstrate that THz emission from whisker-based device is much larger than from crystal-based devices with the same geometry.

Experimental results

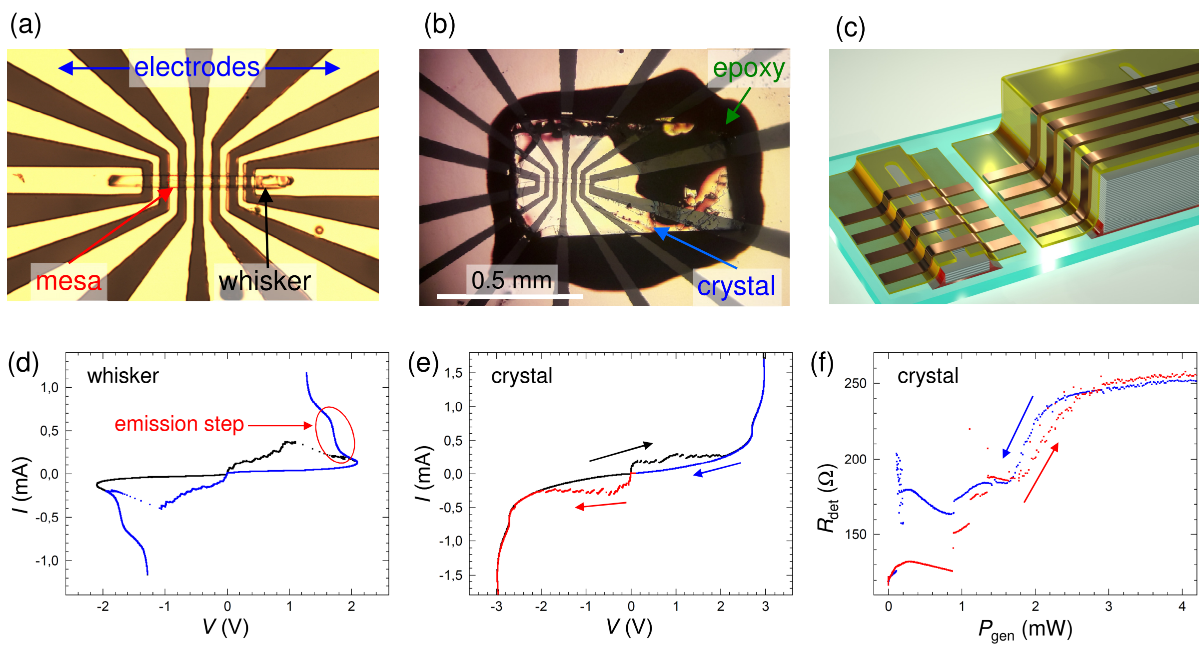

Figure 1: Optical images of (a) whisker and (b) crystal-based devices with similar electrode geometries. (c) A sketch of both devices. Panels (d) and (e) show Current-Voltage characteristics of mesa structures on (d) whisker and (e) crystal-based devices. (f) On-chip generation-detection experiment for the crystal-based device. Here an ac-resistance of the detector mesa is shown as a function of the total dc-dissipation power, $P_{gen} = IV$, of the generator mesa, corresponding to the I-V in (e). The monotonous increment of R_{det} at large P_{gen} corresponds to self-heating. The (small) non-monotonous detector response at $P_{gen} \lesssim 1.5$ mW is due to THz emission from the generator mesa.

Figures 1 (a) and (b) show optical images of two studied devices. They have a similar geometry and were fabricated using the same procedure. The main difference is that the device in (a) is made using a whisker; and in (b) using a conventional large single crystal. Panel (c) shows sketches of both devices. Bi-2212 whiskers have typical aspect ratios 100:10:1 in a, b, and c crystallographic directions [39]. Our whiskers have typical dimensions of several hundreds of microns in a, $20 - 40$ μm in b and just few μm in c-axis direction. In case (b) a big conventional single crystal is used with sizes of almost a mm^2 in the $a - b$ plane and several hundreds of micrometers in the c-axis direction.

The fabrication process starts by gluing a corresponding crystal on a 5×5 mm^2 sapphire substrates using an epoxy glue. The crystal is cleaved at ambient conditions. After that the sample is immediately put into a deposition chamber and a protective gold layer $\sim 60 - 80$ nm is deposited to avoid surface passivation. Next, a line pattern in photoresist is made with the length $100 - 200$ μm and the width $5 - 15$ μm on a flat portion of Bi-2212 surface, followed by Argon ion etching of unprotected parts of Au and Bi-2212, deposition of insulating SiO_2 or CaF_2 layers and a lift-off of the photoresist at the line. The depth of Bi-2212 etching at this stage ($d \sim 200 - 400$ nm) defines the height of mesas and the number of IJJ's in the device, $N = d/s$, where $s \simeq 1.5$ nm is the interlayer spacing between double CuO layers in Bi-2212. After that top metallization Ti/Au layer with the total thickness ~ 200 nm is deposited. Finally several electrodes, crossing the line in a perpendicular direction, are made by photolithography and Ar-ion etching. Mesa structures are formed at the overlap between the line and the electrodes, as indicated in Fig. 1 (a).

Figs. 1 (d) and (e) show current-voltage (I-V) characteristics of mesas at whisker and crystal-based devices, respectively. The I-V's are fairly similar. They contain multiple branches due to one-by-one switching of IJJ's from the superconducting to the resistive state. The number of junctions is ~ 200 for the whisker and ~ 300 for crystal mesas. Both the Bi-2212 crystal and the whisker have similar suppressed $T_c \sim 65 - 70$ K and low critical current densities of IJJs in the mesas, $J_c \sim 100$ A/cm^2. This indicates a strongly underdoped state of Bi-2212 [40].

Radiative properties of our whisker-based devices were analyzed in Ref. [37]. A significant EMW emission at $f \simeq 4.2$ THz with a record-high RPE reaching 12% was reported. The emission occurs at the step in the I-V, marked in Fig. 1 (d). To avoid repetitions we address the reader to Ref. [37] for details.

In Fig. 1 (f) we show results of in-situ THz generation- detection experiment on the crystal-based device from Fig. 1 (b). We follow the procedure developed in Ref. [14], where details of the technique can be found. We use the mesa with the I-V shown in Fig. 1 (e) as a generator, and another mesa nearby as a switching current detector. The detector mesa is biased by a small ac-current and the generator by a dc-current in the same range as in Fig. 1 (e). Fig. 1 (f) shows the ac-resistance of the detector mesa, R_{det}, as a function of the dissipation power in the generator mesa, $P_{gen} = IV$. It is anticipated that self-heating is monotonous (approximately linear) with dissipation power, while the emission is nonmonotonous [14,37] because it occurs at certain bias voltages, corresponding to geometrical resonances in the mesa [14,23,25]. From Fig. 1 (f) it can be seen that there is a general trend for monotonous increment of R_{det} with increasing P_{get}, which is the consequence of crystal heating. On top of it there is a small non-monotonous signal at 0.5 mW $\lesssim P_{gen} \lesssim$ 1.5 mW, which can be attributed to THz emission. This is qualitatively similar to results reported earlier for small mesas on crystal-based devices [14]. For whisker-based mesas the ratio of emission to self-heating responses is quantitatively different: The emission peak $R_{det}(P_{get})$ is much larger than the monotonous self-heating background (see Fig. 2 (a) in Ref. [37]). Since the dissipation power is similar for both devices (see Fig. 3 (f) in Ref. [37]), this indicates a much larger RPE in the whisker-based device.

Numerical results

To understand the reported difference between crystal and whisker-based devices and to suggest possible optimizations of THz sources, we performed numerical modelling using Comsol Multiphysics. Below we present simulations of thermal and radiative properties calculated using Heat Transfer and RF modules, respectively.

Modelling of heat transfer

Generally, analysis of self-heating in Bi-2212 mesas is a complex non-linear problem [27,29-31,33, 35]. Simulations presented below are made for the base temperature T_0 = 10 K and for sizes similar to the actual devices, shown in Fig. 1: substrate size $5 \times 5 \times 0.3$ mm^3, crystal size $1 \times 1 \times 0.3$ mm^3, whisker size $300 \times 30 \times 3$ μm^3 and mesa size $30 \times 30 \times 0.3$ μm^3. Epoxy layer beneath the Bi-2212 crystal is 1 μm thick. The monocrystalline sapphire substrate has a very good thermal conductivity, κ, at low T. The substrate is well thermally anchored with the boundary condition at the bottom surface $T = T_0$. Due to the good thermal conductivity, the temperature variation in the substrate is negligible and we may neglect its $\kappa(T)$ dependence. Therefore, we use $\kappa = 3000$ W/K^{-1}m^{-1} for the sapphire substrate at $T \sim 10$ K [41]. To the contrary, the epoxy used for gluing Bi-2212 crystals, has a poor heat conductance at low T. We do not consider its T-dependence because it acts just as a heat blocking layer, which we assume to have $\kappa = 0.0025$ W/K^{-1}m^{-1}. On the other hand, it is necessary to take into account actual $\kappa(T)$ dependencies for the other two materials, Bi-2212 and polycrystalline gold electrodes. At low T both have linear $\kappa(T)$. For Bi-2212 we assume $\kappa(T) = 0.1\ T(\mathrm{K})$ W/K^{-1}m^{-1} [42] with an anisotropy $\kappa_{ab}/\kappa_c = 8$ [43]. For a polycrystalline gold thin film we use $\kappa(T) = 3\ T(\mathrm{K})$ W/K^{-1}m^{-1} [31]. The heat is introduced via a dissipation power of 1 mW with a constant density in the mesa volume.

Figure 2 represents heat-transfer simulations for a whisker without an electrode. Panels (a) and (b) show sketches of the device and the x-z cross-section through the mesa (not in scale). Figs. (c-e) show the temperature distribution for the case when the sample is placed in vacuum: (c) top view, (b) x-z cross-section through the mesa (stretched by a factor 3 in the vertical direction), and (e) T-distribution in the mesa (stretched by a factor 50 in the vertical direction). In this case the heat can only sink into the substrate. As seen from Fig. 2(d), the epoxy layer between the substrate and the whisker blocks heat flow into the substrate and causes a substantial heating of the whole whisker with the maximum temperature in the center of the mesa reaching T_{max} = 85.2 K. Figs. 2(f-h) show simulations for the same device in the exchange ^{4}He gas. Clearly, it helps to cool down the device, although self-heating still remains substantial, T_{max} = 56.7 K.

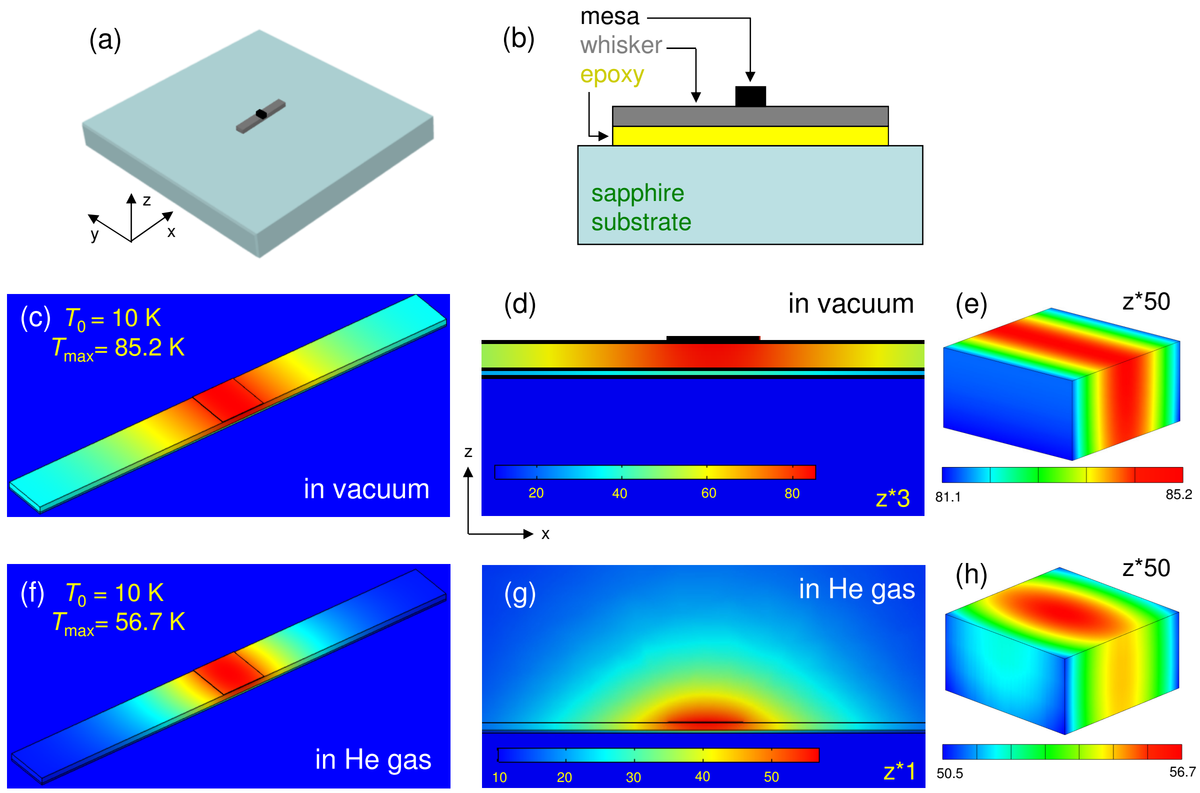

Figure 2: Heat transport in a whisker-based device without electrodes. (a) A sketch of the device and (b) a cross-section through the mesa (not in scale). (b-e) Calculated temperature distribution for the device in vacuum. (f-h) The same for the device in exchange He gas.

Figure 3 represents simulations for the whisker-based device with the top Au electrode. Outside the whisker the electrode is in a direct contact with the sapphire substrate (no epoxy). This creates a good thermal sink and, as a result, T_{max} falls to $\sim$ 23 K. Addition of the exchange gas doesn't play a major role in this case because the main heat sink channel is provided by the electrode, acting as a heat spreading layer [28].

Figure 4 shows temperature distribution in a crystal-based device in vacuum (a) without electrodes and (b) with electrodes. The main difference is that unlike in the whisker-device, Fig. 2, there is no major temperature jump in the epoxy layer between the crystal and the substrate. This occurs because the heat resistance of the epoxy layer is inversely proportional to the total in-plane x-y area. Due to a much larger crystal area this heat resistance is negligible, despite a poor heat conductivity of epoxy. Adding an electrode and He exchange gas further reduces self-heating, but their effect is not as profound as for the whisker-device, Fig. 3, due to the effective heat sink channel into the

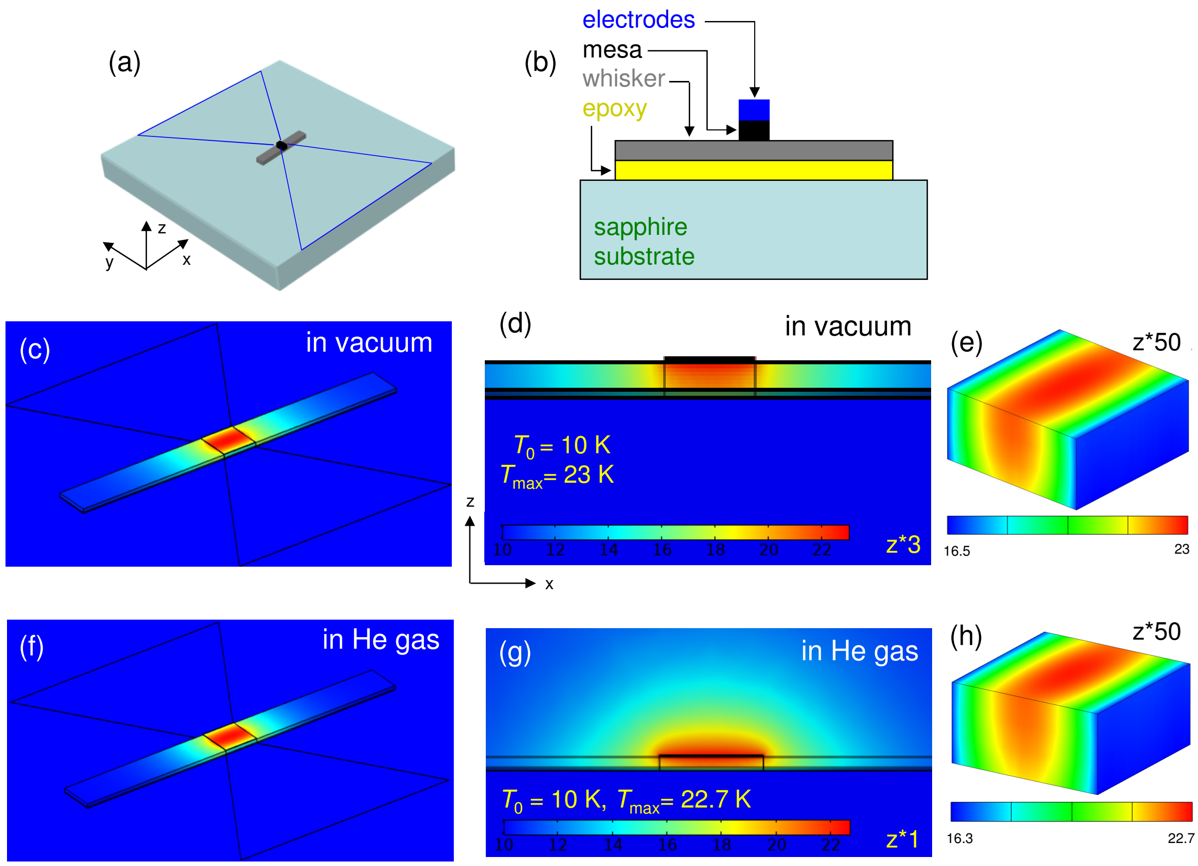

Figure 3: Heat transport in a whisker-based device with an electrode. (a) A sketch of the device and (b) a cross-section through the mesa (not in scale). (b-e) Calculated temperature distribution for the device in vacuum. (f-h) The same for the device in exchange He gas.

substrate. Of course, the effectiveness of this channel depends on the thickness of the epoxy layer. In simulations above we assumed a fixed thickness of 1 μm both for the whisker and the large crystal. However, in reality the thickness depends on the quantity of applied epoxy. Significantly larger quantities are required for gluing large crystals, which, due to capillary forces, results in a larger thickness of epoxy. Concurrently thinner than 1μm epoxy layers can be achieved for gluing tiny whiskers. Therefore, the extent of self-heating in our simulations, Figs. 2, 3 and 4, is only indicative. For a real device it will depend on the actual geometry, sizes and thicknesses.

Modelling of radiative properties

For calculation of THz properties, a mesa (the source) is modelled as a lumped port with a fixed voltage amplitude. Unlike the heat transfer problem, this problem is linear so that the results di-

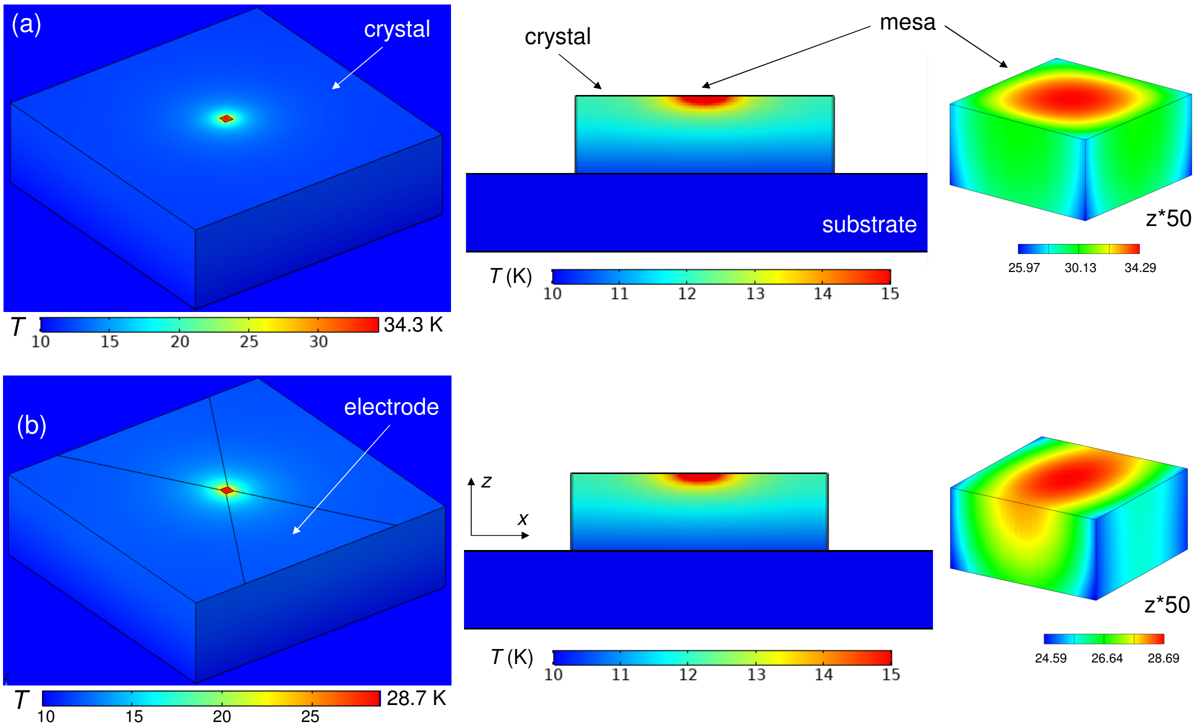

Figure 4: Heat transport in a crystal-based device in vacuum (a) without electrodes, (b) with electrodes. Left panel represent top views, middle panels - the x-z cross-section through the mesa, and right panels the mesa (expanded by factor 50 in z-direction).

rectly scale with the source amplitude. To simplify the perception, we use the amplitude of 1 Volt. Simulations are made in a sphere with the radius, R, which is chosen to be at least two times larger than the largest device size and the wavelength in vacuum. A perfectly matching layer with the thickness 0.1 R is added outside the sphere to avoid reflections. We checked that the presented results do not depend on R and, therefore, properly describe far-field characteristics.

Figure 5 represents radiative characteristics for three device geometries, sketched in the leftmost panels: (a) a mesa (red) on a large crystal (black) with an attached metallic electrode (yellow), mounted on a dielectric substrate; (b) a mesa on a large crystal with a capping metallic layer, without electrode; (c) a mesa on a thin whisker (black) with an attached electrode. Simulations are performed for $f = 1$ THz and the sizes are selected relative to the wavelength in vacuum, $\lambda_1 = 300\ \mu$m: the substrate and the in-plane crystal size, whisker and electrode lengths are $\lambda_1/2 = 150\ \mu$m; the substrate height is $\lambda_1/4 = 75\ \mu$m; the in-plane mesa size, whisker and electrode widths are $\lambda_1/8 = 37.5\ \mu$m; the crystal height is $\lambda_1/10 = 30\ \mu$m; mesa and whisker

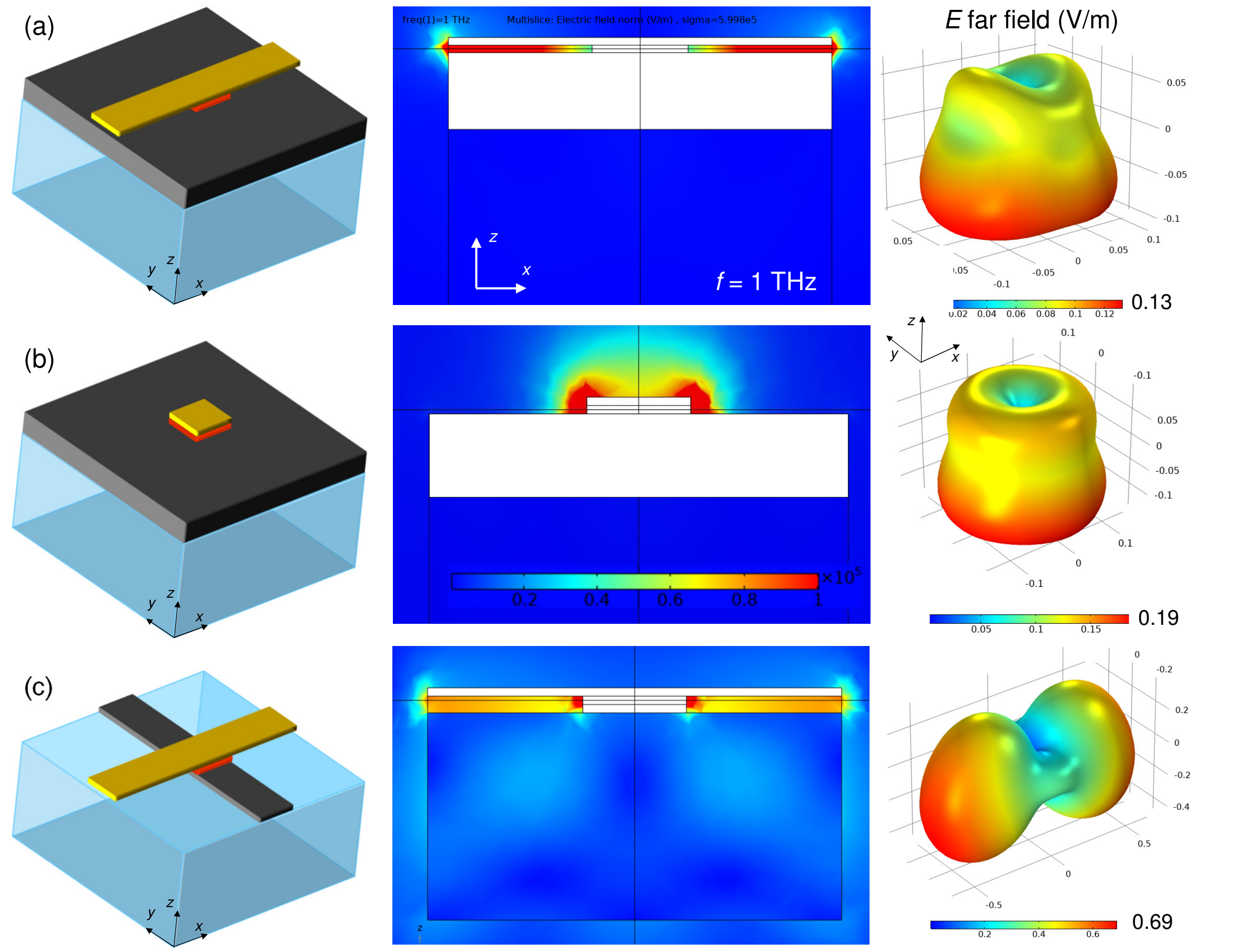

Figure 5: Simulated radiative properties at $f = 1$ THz for (a) crystal based device, (b) crystal-based device without electrodes, and (c) whisker-based device. Left panels show sketches of devices; middle panels - electric field amplitudes in the x-z cross-section through the mesa; right panels represent radiation patterns for the electric field amplitude in the far-field (outside the simulation sphere). Note a strong field concentration between the crystal and the electrode in (a).

heights, the electrode thickness is $\lambda_1/100 = 3$ μm; the simulation sphere radius $R = 2\lambda_1$ and the perfectly matching layer thickness 0.2 λ_1. The sizes and parameters are chosen to be similar (but not identical) to studied samples in order to optimize the mesh size and the calculation time. Therefore, such simulations serve for a qualitative illustration of the difference between crystal and whisker-based devices and the role of the electrodes. Electrode and whisker conductivity is set to $\simeq 6 \times 10^5$ $(\Omega m)^{-1}$ and relative dielectric permittivity of the substrate $\epsilon_r = 10$. Dielectric losses are not considered, $\tan(\delta) = 0$. Middle panels in Fig. 5 show local distributions of electric field amplitudes in the $x - z$ cross-section, going through the mesa. The same color scale is used, indicated in the middle panel of Fig. 5 (b). Rightmost panels represent far-field radiation patterns (directionality diagrams) of the electric field amplitude outside the simulation sphere.

From comparison of middle panels in Figs. 5 (a) and (c) it can be seen that the electric field distribution is significantly different. In the crystal-based device the field is locked between the electrode and the crystal. This occurs because the electrode is laying on top of the crystal, forming together a parallel plate capacitor. The field is trapped inside this capacitor and does not go neither in the substrate, nor open space in the top hemisphere (with exception of small stray fields). If we take a realistic specific capacitance $C_{\square} \sim 1$ fF/μm^2 and electrode area 37.5×150 μm^2, we obtain for $f = 1$ THz that the capacitive impedance is very small $|Z_C| = 1/2\pi f C \simeq 0.03\ \Omega$, much smaller that the wave impedance of the free space, $Z_0 = \sqrt{\mu_0/\epsilon_0} \simeq 377\ \Omega$. This leads to trapping of EMW in the electrode/crystal capacitance, which shunts open space and prevents emission.

To the contrary, for the whisker-based device, Fig. 5 (c), the field goes out of the mesa as can be seen from the brighter overall tone of the pattern in the middle panel. The EMW propagation is particularly well seen in the bottom hemisphere due to formation of a standing wave pattern in the substrate. It is induced by reflections at the substrate/vacuum interfaces caused by a significant difference in refractive indices. Emission of EMW is associated with a cross-like structure of the whisker device, as sketched in the leftmost panel of Fig. 5 (c). It obviates direct overlap of the whisker and the electrode and prevents appearance of the large parasitic capacitance. This cross-like structure resembles the turnstile (crossed-dipole) antenna geometry, which facilitates good impedance matching with open space.

The difference between crystal and whisker-based devices is also reflected in the far-fields characteristics, shown in the rightmost panels of (a) and (c). The maxim field amplitudes, E_{max}, marked in bottom right corners, are significantly different: 0.13 V/m for crystal and 0.69 V/m for whisker-based device. Since the emitted power is proportional to E_{max}^2, the RPE of the whisker-based device is almost 30 times larger than for the crystal-based. This indicates a good impedance matching of the whisker device and a poor matching for the crystal device. To further demonstrate the detrimental role of the parasitic electrode/crystal capacitor, in Fig. 5 (b) we considered the case with a mesa on a crystal without electrode and only with the capping top layer on the mesa. Such configuration is relevant for large mesas, contacted by a bonding wire [9]. Remarkably, the far-field emission is larger, $E_{max} = 0.19$ V/m, in the absence of the electrode. This clearly shows that the electrode on top of the crystal does not help in impedance matching. To the contrary, it makes things worse due to formation of the large parasitic capacitance, shunting the EMW.

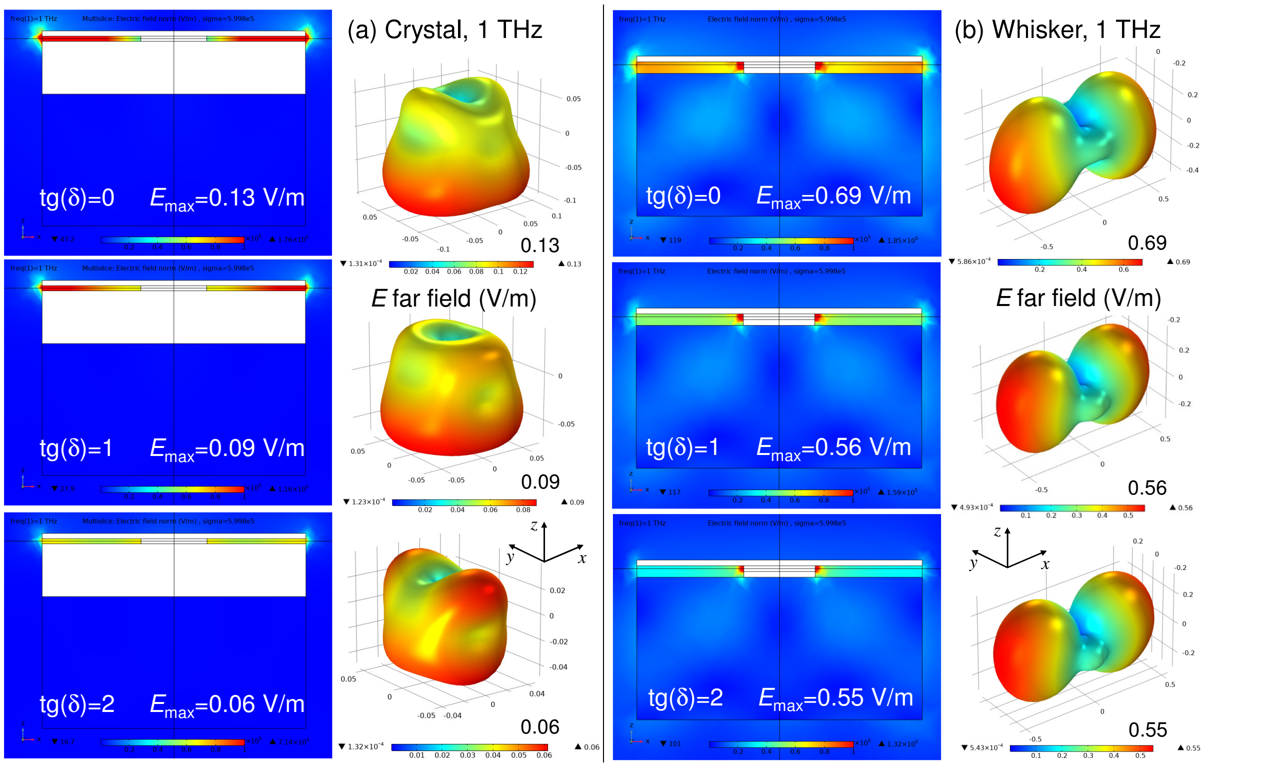

Figure 6: Variation of radiative properties with increasing dielectric losses $\tan(\delta) = 0$ (top row), 1 (middle row), and 2 (bottom row) for (a) crystal-based (two leftmost columns) and (b) whisker-based devices (two rightmost columns). Simulations are made at $f = 1$ THz. Note a rapid suppression of the far-field amplitudes in crystal-based devices.

Simulations presented in Fig. 5 are made for ideal dielectrics with zero dielectric losses, $\tan(\delta) = 0$. The detrimental role of the parasitic crystal/electrode capacitance becomes much more pronounced if we take into account dielectric losses, which can be significant at THz frequencies. In Figure 6 we show variation of radiative properties of (a) crystal-based and (b) whisker based devices upon increasing dielectric losses in the insulating layer between the crystal and the electrode for crystal-based device and substrate and electrode for whisker-based device: $\tan(\delta) = 0$ (top), $\tan(\delta) = 1$ (middle), and $\tan(\delta) = 2$ (bottom row of panels). It is seen that for whisker-based device dielectric losses only slightly reduce E_{max} from 0.69 V/m for $\tan(\delta) = 0$ to 0.55 V/m for $\tan(\delta) = 2$. For crystal-based device the relative reduction is significantly larger, from 0.13 V/m for $\tan(\delta) = 0$ to 0.06 V/m for $\tan(\delta) = 2$. As a result, the ratio of RPE for whisker and crystal devices increases from $\sim$ 28 for $\tan(\delta) = 0$, to $\sim$ 39 for $\tan(\delta) = 1$ and $\sim$ 84 for $\tan(\delta) = 2$. This is a direct consequence of electric field concentration in the parasitic crystal/electrode capacitance of crystal-based devices.

Discussion

Josephson oscillators can provide unprecedented tunability in the whole THz range at a primary frequency [14]. However, being cryogenic devices, they are susceptible to self-heating, which limits both the achievable frequency range and the emission power. As pointed out in Ref. [37], the maximum emission power is limited by the cooling power of the device and the radiation power efficiency:

$$P_{THz} < P_{cooling} \times RPE. \tag{1}$$

Enhancement of the effective cooling power requires implementation of special cooling elements at the device. Despite a significant progress in this direction [10,12,13,32,33,35,44], it is unlikely that a single emitter would be able to sustain the dissipation power above few tens of mW. The tolerable dissipation power can be significantly enhanced by spreading it between several smaller emitters [10,19] because smaller mesa structures are less prone to self-heating [14,27,28,30]. Such a strategy has been successfully proved for arrays of Josephson junctions [45-47], for which coherent emission from up to 9000 synchronized junctions was reported [46]. Yet, the ultimate dissipation power is limited by the cooling power of the cryostat itself. For compact cryorefrigerators it is in the range of 100 mW. As follows from Eq. (1), the source with RPE= 1% (which is good for THz sources) would not be able to emit more than $P_{TH_z} = 1$ mW. Therefore, further enhancement of the emission power requires enhancement of RPE. This in turn requires proper microwave design to facilitate impedance matching with open space. The maximum RPE in case of perfect matching is 50% [38], implying that up to 50 mW emitted THz power could be achieved.

Above we considered design aspects of THz sources, which contribute to obviation of self-heating and improvement of impedance matching. Several geometries of Bi-2212 devices were analyzed. It is shown that geometries of both the Bi-2212 crystal and the electrodes are playing important roles. Their effect, however, depends on the device type.

For crystal-based devices (using large crystals $\sim$ 1 mm^2 in the ab-plane, see Fig. 1 (b)) the size of the crystal is playing opposite roles in device operation. On the one hand, a large ab-plane area helps to spread heat into the substrate and reduces self-heating of the device, as seen from Fig. 4. On the other hand, it leads to a large overlap area between the crystal and the top electrode. This creates a large parasitic capacitance that shunts THz emission and suppresses RPE.

In whisker-based devices the situation is different. Here the electrode provides the main heat sink channel, as shown in Fig. 3. The cross-like geometry prevents an overlap between the whisker and the electrode, thus obviating the parasitic capacitance. Furthermore, the long whisker and the electrode act as two arms of the crossed dipole (turnstile) antenna, facilitating good impedance matching with open space.

The role of the substrate is also different. In crystal-based devices the large superconducting crystal screens the EMW, so that there is practically no field in the substrate, see Figs. 5 (a) and (b). In this case the substrate does not influence radiative properties. To the contrary, for whisker-based device a significant fraction of EMW is going into the substrate due to its larger dielectric constat. The difference of dielectric constants of the substrate and vacuum leads to internal reflections and formation of standing waves in the substrate, see Fig. 5 (c). Therefore, the substrate acts as a dielectric resonator and may strongly affect the radiation pattern of the device.

Presented numerical simulations provide a qualitative explanation of the reported difference in radiative properties of whisker and crystal-based devices, shown in Figs. 1 (a) and (b). They explain why RPE of whisker-based devices is much larger (by more that an order of magnitude, as follows from Fig. 6). Those conclusions are in agreement with experimentally reported RPE, which is in the range of $\lesssim 1\%$ for crystal-based [10,14] and up to 12% for whisker-based [37] devices.

Conclusions

To conclude, intrinsic Josephson junctions in layered high-temperature superconductor Bi-2212 can provide an alternative technology for creation of tunable THz sources. In this work we analyzed two main phenomena that limit performance of such devices: self-heating and low RPE caused by impedance mismatching. We presented numerical simulations of thermal and radiative properties of Bi-2212 THz sources based on conventional large single crystals and needle-like whiskers. Simulations are performed for various geometrical configurations and parameters. A comparison with experimental data for crystal and whisker-based devices is made. It is demonstrated that the structure and the geometry of both the superconductor and the electrodes are playing important roles. Crystal-based devices suffer from a large parasitic capacitance due to an overlap between the crystal and the electrodes. This prevents good impedance matching and reduces RPE. The overlap is avoided in whisker-based devices. Moreover, the whisker and the electrodes forms a turnstile (crossed-dipole) antenna facilitating good impedance matching with open space. Our simulations demonstrate that this may enhance the radiation power efficiency in whisker-based devices by more than an order of magnitude compared to crystal-based devices, which is consistent with the experimental data.

Acknowledgements

We are grateful to A. Agostino and M. Truccato for assistance with whisker preparation and to A. Efimov and K. Shiianov for assistance in experiment.

Funding

The work was supported by the Russian Science Foundation Grant No. 19-19-00594. The manuscript was written during a sabbatical semester of V. M. K. at MIPT, supported by the Faculty of Sciences at SU.

References

1. Tonouchi, M. *Nature Photonics* **2007**, *1*, 97–105.

2. Razeghi, M.; Lu, Q. Y.; Bandyopadhyay, N.; Zhou, W.; Heydari, D.; Bai, Y.; Slivken, S. *Optics Express* **2015**, *23*, 229245.

3. Belkin, M. A.; Capasso, F. *Phys. Scripta* **2015**, *90*, 118002.

4. Wang, X.; Shen, C.; Jiang, T.; Zhan, Z.; Deng, Q.; Li, W.; Wu, W.; Yang, N.; Chu, W.; Duan, S. *AIP Advances* **2016**, *6*, 075210.

5. Curwen, C. A.; Reno, J. L.; Williams, B. S. *Nature Photonics* **2019**, *13*, 855.

6. Walther, C.; Fischer, M.; Scalari, G.; Terazzi, R.; Hoyler, N.; Faist, J. *Appl. Phys. Lett.* **2007**, *91*, 131122.

7. Vijayraghavan, K.; Jiang, Y.; Jang, M.; Jiang, A.; Choutagunta, K.; Vizbaras, A.; Demmerle, F.; Boehm, G.; Amann, M.; Belkin, M. *Nature Commun.* **2013**, *4*, 2021.

8. Rösch, M.; Scalari, G.; Beck, M.; Faist, J. *Nature Photonics* **2015**, *9*, 42–47.

9. Ozyuzer, L.; Koshelev, A. E.; Kurter, C.; Gopalsami, N.; Li, Q.; Tachiki, M.; Kadowaki, K.; Yamamoto, T.; Minami, H.; Yamaguchi, H.; Tachiki, T.; Gray, K. E.; Kwok, W.-K.; Welp, U. *Science* **2007**, *318*, 1291.

10. Benseman, T. M.; Gray, K. E.; Koshelev, A. E.; Kwok, W.-K.; Welp, U.; Minami, H.; Kadowaki, K.; Yamamoto, T. *Appl. Phys. Lett.* **2013**, *103*, 022602.

11. Welp, U.; Kadowaki, K.; Kleiner, R. *Nature Photonics* **2013**, *7*, 702.

12. Kashiwagi, T.; Yamamoto, T.; Minami, H.; Tsujimoto, M.; Yoshizaki, R.; Delfanazari, K.; Kitamura, T.; Watanabe, C.; Nakade, K.; Yasui, T.; Asanuma, K.; Saiwai, Y.; Shibano, Y.; Enomoto, T.; Kubo, H.; Sakamoto, K.; Katsuragawa, T.; Marković, B.; Mirković, J.; Klemm, R.; Kadowaki, K. *Phys. Rev. Appl.* **2015**, *4*, 054018.

13. Zhou, X.; Zhu, Q.; Ji, M.; An, D.; Hao, L.; Sun, H.; Ishida, S.; Rudau, F.; Wieland, R.; Li, J.; Koelle, D.; Eisaki, H.; Yoshida, Y.; Hatano, T.; Kleiner, R.; Wang, H.; Wu, P. *Appl. Phys. Lett.* **2015**, *107*, 122602.

14. Borodianskyi, E.; Krasnov, V. *Nat. Commun.* **2017**, *8*, 1742.

15. Sun, H.; Wieland, R.; Xu, Z.; Qi, Z.; Lv, Y.; Huang, Y.; Zhang, H.; Zhou, X.; Li, J.; Wang, Y.; Rudau, F.; Hampp, J.; Koelle, D.; Ishida, S.; Eisaki, H.; Yoshida, Y.; Jin, B.; Koshelets, V.; Kleiner, R.; Wang, H.; Wu, P. *Phys. Rev. Appl.* **2018**, *10*, 024041.

16. Kashiwagi, T.; Yuasa, T.; Tanabe, Y.; Imai, T.; Kuwano, G.; Ota, R.; Nakamura, K.; Ono, Y.; Kaneko, Y.; Tsujimoto, M.; Minami, H.; Yamamoto, T.; Klemm, R.; Kadowaki, K. *J. Appl. Phys.* **2018**, *124*, 033901.

17. Zhang, H.; Wieland, R.; Chen, W.; Kizilaslan, O.; Ishida, S.; Han, C.; Tian, W.; Xu, Z.; Qi, Z.; Qing, T.; Lv, Y.; Zhou, X.; Kinev, N.; Ermakov, A.; Dorsch, E.; Ziegele, M.; Koelle, D.; Eisaki, H.; Yoshida, Y.; Koshelets, V.; Kleiner, R.; Wang, H.; Wu, P. *Phys. Rev. Appl.* **2019**, *11*, 044004.

18. Kuwano, G.; Tsujimoto, M.; Kaneko, Y.; Imai, T.; Ono, Y.; Nakagawa, S.; Kusunose, S.; Minami, H.; Kashiwagi, T.; Kadowaki, K.; Simsek, Y.; Welp, U.; Kwok, W.-K. *Phys. Rev. Appl.* **2020**, *13*, 014035.

19. Tsujimoto, M.; Fujita, S.; Kuwano, G.; Maeda, K.; Elarabi, A.; Hawecker, J.; Tignon, J.; Mangeney, J.; Dhillon, S.; Kakeya, I. *Phys. Rev. Appl.* **2020**, *13*, 051001.

20. Saiwai, Y.; Kashiwagi, T.; Nakade, K.; Tsujimoto, M.; Minami, H.; Klemm, R.; Kadowaki, K. *Jpn. J. Appl. Phys.* **2020**, *59*, 105004.

21. Delfanazari, K.; Klemm, R. A.; Joyce, H. J.; Ritchie, D. A.; Kadowaki, K. *Proc. IEEE* **2020**, *108*, 721–734.

22. Kleiner, R.; Müller, P. *Phys. Rev. B* **1994**, *49*, 1327.

23. Krasnov, V. M.; Mros, N.; Yurgens, A.; Winkler, D. *Phys. Rev. B* **1999**, *59*, 8463–8466.

24. Katterwe, S. O.; Krasnov, V. M. *Phys. Rev. B* **2009**, *80*, 020502(R).

25. Katterwe, S. O.; Rydh, A.; Motzkau, H.; Kulakov, A. B.; Krasnov, V. M. *Phys. Rev. B* **2010**, *82*, 024517.

26. Krasnov, V. M.; Yurgens, A.; Winkler, D.; Delsing, P.; Claeson, T. *Phys. Rev. Lett.* **2000**, *84*, 5860.

27. Krasnov, V. M. *Phys. Rev. B* **2009**, *79*, 214510.

28. Krasnov, V. M.; Yurgens, A.; Delsing, P. *J. Appl. Phys.* **2001**, *89*, 5578.

29. Krasnov, V. M. *Physica C* **2002**, *372–376*, 103–106.

30. Krasnov, V. M.; Bauch, T.; Delsing, P. *Phys. Rev. B* **2005**, *72*, 012512.

31. Yurgens, A. *Phys. Rev. B* **2011**, *83*, 184501.

32. Asai, H.; Kawabata, S. *Appl. Phys. Lett.* **2014**, *104*, 112601.

33. Rudau, F.; Tsujimoto, M.; Gross, B.; Judd, T. E.; Wieland, R.; Goldobin, E.; Kinev, N.; Yuan, J.; Huang, Y.; Ji, M.; Zhou, X. J.; An, D. Y.; Ishii, A.; Mints, R. G.; Wu, P.; Hatano, T.; Wang, H. B.; Koshelets, V. P.; Koelle, D.; Kleiner, R. *Phys. Rev. B* **2015**, *91*, 104513.

34. Benseman, T. M.; Koshelev, A. E.; Vlasko-Vlasov, V.; Hao, Y.; Kwok, W.-K.; Welp, U.; Keiser, C.; Gross, B.; Lange, M.; Koelle, D.; Kleiner, R.; Minami, H.; Watanabe, C.; Kadowaki, K. *Phys. Phys. Appl.* **2015**, *3*, 044017.

35. Rudau, F.; Wieland, R.; Langer, J.; Zhou, X. J.; Ji, M.; Kinev, N.; Hao, L. Y.; Huang, Y.; Li, J.; Wu, P. H.; Hatano, T.; Koshelets, V. P.; Wang, H. B.; Koelle, D.; Kleiner, R. *Phys. Rev. Appl.* **2016**, *5*, 044017.

36. Oikawa, D.; Mitarai, H.; Tanaka, H.; Tsuzuki, K.; Kumagai, Y.; Sugiura, T.; Andoh, H.; Tsukamoto, T. *AIP Adv.* **2020**, *10*, 085113.

37. Cattaneo, R.; Borodianskyi, E. A.; Kalenyuk, A. A.; Krasnov, V. M. *ArXiV:2109.00976* **2021**.

38. Krasnov, V. M. *Phys. Rev. B* **2010**, *82*, 134524.

39. Matsubara, I.; Kageyama, H.; Tanigawa, H.; Ogura, T.; Yamashita, H.; Kawai, T. *Japan. J. Appl. Phys. Part 2* **1989**, *28*, L1121.

40. Jacobs, T.; Simsek, Y.; Koval, Y.; Müller, P.; Krasnov, V. M. *Phys. Rev. Lett.* **2016**, *116*, 067001.

41. Dobrovinskaya, E. R.; Lytvynov, L. A.; Pishchik, V. Properties of Sapphire. In *Sapphire. Materials, Manufacturing, Applications*; Springer Science + Business Media, LLC: New York, USA, 2009; pp 109–114.

42. Zavaritsky, N. V.; Samoilov, A. V.; Yurgens, A. A. *Physica C* **1991**, *180*, 417–425.

43. Crommie, M. F.; Zettl, A. *Phys. Rev. B* **1991**, *43*, 408–412.

44. Ji, M.; Yuan, J.; Gross, B.; Rudau, F.; An, D. Y.; Li, M. Y.; Zhou, X. J.; Huang, Y.; Sun, H. C.; Zhu, Q.; Li, J.; Kinev, N.; Hatano, T.; Koshelets, V. P.; Koelle, D.; Kleiner, R.; Xu, W.; Jin, B.; Wang, H.; Wu, P. *Appl. Phys. Lett.* **2014**, *105*, 122602.

45. Barbara, P.; Cawthorne, A. B.; Shitov, S. V.; Lobb, C. J. *Phys. Rev. Lett.* **1999**, *82*, 1963–1966.

46. Galin, M. A.; Borodianskyi, E. A.; Kurin, V. V.; Shereshevskiy, I. A.; Vdovicheva, N. K.; Krasnov, V. M.; Klushin, A. M. *Phys. Rev. Appl.* **2018**, *9*, 054032.

47. Galin, M. A.; Rudau, F.; Borodianskyi, E. A.; Kurin, V. V.; Koelle, D.; Kleiner, R.; Krasnov, V. M.; Klushin, A. M. *Phys. Rev. Appl.* **2020**, *14*, 024051.